

# Characterising Instrumentation Canister Aerodynamics on the FAAM BAe-146-301 Atmospheric Research Aircraft

C J Bennett<sup>1</sup>, G J Nott<sup>2</sup>, A Wellpott<sup>3</sup>, N Lawson<sup>4</sup>, M Delise<sup>5</sup>, B Woodcock<sup>6</sup>, and G B Gratton<sup>7</sup>

<sup>1</sup>National Flying Laboratory Centre, School of Aerospace, Transport and Manufacturing,  
Cranfield University, UK., Email: C.J.Bennett@Cranfield.ac.uk

<sup>2</sup>Facility for Airborne Atmospheric Measurements (FAAM), Bedfordshire, UK

<sup>3</sup>Facility for Airborne Atmospheric Measurements (FAAM), Bedfordshire, UK

<sup>4</sup>National Flying Laboratory Centre, School of Aerospace, Transport and Manufacturing,  
Cranfield University, UK.

<sup>5</sup>National Flying Laboratory Centre, School of Aerospace, Transport and Manufacturing,  
Cranfield University, UK.

<sup>6</sup>Aventech Research Inc, Ontario, Canada

<sup>7</sup>Facility for Airborne Atmospheric Measurements (FAAM), Bedfordshire, UK

## ABSTRACT

A Computational Fluid Dynamic (CFD) investigation is aimed at accurately predicting the air flow characteristics in the vicinity of under-wing mounted instruments on the Facility for Airborne Atmospheric Measurement's (FAAM) BAe-146-301. Perturbation of the free stream airflow as it passes through the region of detection of the under-wing instruments, may lead to additional uncertainties in the measurement of clouds and cloud particles. The CFD model was validated with flight data from an Aircraft-Integrated Meteorological Measurement System (AIMMS-20) in a wing-mounted instrument canister. Flow predictions show a consistent slowing from the true air speed of the aircraft in the longitudinal direction and horizontal and vertical flows up to 10% of the air speed being introduced. The potential impact of these flow perturbations on sizing of particles

with Cloud Imaging Probes is modelled. Sizing errors are dependent on the methodology used and the shape of the particle, those due to transverse flows remain very small but miss-sizing due to unaccounted longitudinal flow perturbations are potentially more serious.

## Acknowledgements

Airborne data was obtained using the BAe-146-301 Atmospheric Research Aircraft flown by Airtask Ltd and managed by the Facility for Airborne Atmospheric Measurements (FAAM), which is a joint entity of the Natural Environment Research Council (NERC) and the UK Met Office.

## INTRODUCTION

The Facility for Airborne Atmospheric Measurements (FAAM) is a publicly funded research facility that, as part of the National Centre for Atmospheric Science (NCAS), supports atmospheric research in the United Kingdom by providing an instrumented large atmospheric research aircraft (ARA) and associated services. The ARA is a BAe-146-301 aircraft, registration G-LUXE, owned by the National Environment Research Council and flown by Airtask Group Ltd. The aircraft has been extensively modified to carry 19” rack-based instruments within the cabin, canister-based instruments affixed to underwing pylons, and remote sensing instruments carried on the roof, belly, and inside a blister affixed to the port side of the fore section of the fuselage. The exact instrument fit changes based on the scientific objectives of each flight. The aircraft carries 3 crew and up to 18 scientists who operate the research equipment.

This study focuses on the instrument cluster mounted on the underside of the port wing, see Fig. 1 which shows four different probes fitted in the four canister positions. In the upper-outer position is the Cloud Imaging Probe (CIP100), in the upper-inner position is the Passive Cavity Aerosol Spectrometer Probe (PCASP), the lower-inner canister houses the Cloud Droplet Probe (CDP) all manufactured by Droplet Measurement Technologies Inc, and in the lower-outer position is the Aircraft-Integrated Meteorological Measurement System (AIMMS-20) by Aventech Research Inc. The PCASP, CDP, and CIP100 measure aerosol and cloud particles over nominal size ranges of 0.1–3 $\mu$ m, 3–50 $\mu$ m, and 100-6200 $\mu$ m respectively. The AIMMS samples meteorological data

(temperature, humidity and pressure data), aircraft attitude data, and 3-dimensional winds with a 5-port probe positioned on a 0.425m boom.

The aim of this paper is to investigate the air flow characteristics within the measurement zone of the open-path instruments, for example the CIP100 and CDP as shown in Fig. 1. Due to the inertia of larger hydrometeors such as cloud and precipitation particles, these particles must be measured by open-path instruments mounted on booms or pylons rather than with cabin-based instruments which require inlets on the aircraft's skin Wilson and Jonsson (2011). The open-path instruments discussed in this work are laser based imaging probes which record particle shadows on a one-dimensional detector array as they pass through the sample volume. A broad range of particle sizes from tens of micrometres to several centimetres may be measured by this type of instrument.

There are a number of factors which can affect the air flow characteristics within the measurement zone of open-path instruments. The redirection/deflection of air flow around the airframe (including the instrument cluster itself), congestion/compression of the airflow immediately upstream of the instrument Weigel et al. (2016); Korolev et al. (2012), pressure gradients generated by lifting surfaces such as the wings, and pressure gradients generated by the engines may all affect the air flow direction/angle, speed, and quality (laminar/turbulent) in the instrument's measurement zone.

Firstly, if the flow direction through the sample volume is altered, imaged particles may appear uniformly skewed at an angle. MacPherson and Baumgardner MacPherson and Baumgardner (1988) demonstrate this in a study of a Beechcraft King Air. It is shown that a transverse flow skews particles proportionally to the ratio of transverse to longitudinal flow speeds. This effect is dependent on particle inertia, related to the size of each particle Twohy and Rogers (1993), and hence will skew the measured particle size distribution.

Secondly, the speed of air through the instrument sample volume or probe air speed (PAS) is important as it is used, when combined with the two dimensional sample area as defined by the laser geometry, to convert an internal clock time step into a volumetric flow rate. Then, with the number

of particles in a given time interval counted, a volumetric number concentration of particles can be calculated. Hence, if the PAS diverges from the aircraft true air speed (TAS), and this is not accounted for, the measured number concentration may be affected Korolev et al. (2012).

Finally, convergence and divergence of flow lines may also change the concentration of particles passing through the probe's sample volume relative to the ambient concentration Twohy and Rogers (1993). Again, this effect is dependent on the inertia for a range of particle sizes.

Therefore, understanding the air flow characteristics at different flight conditions may allow the deviations in measured particle population, compared to the unperturbed ambient, to be compensated for. At the very least, the impact on the uncertainty of the measurements will be revealed. Clearly, these features are highly aircraft/instrument specific, but are analysed here for a BAe-146 as an example of the methodology which can be employed to better understand the performance and correlation of instruments used in atmospheric research.

Flow modelling for the aircraft was done during the initial conversion of the aircraft for its current atmospheric research role using a very simplified shape representation and standard Engineering Sciences Data Unit (ESDU) data sheets. However, these have not the required precision, particularly around the wing pylons, to quantify the effects of flows on particle measurements. In 2015 the aircraft was laser scanned to provide the basis for a Computational Fluid Dynamics (CFD) model of the aircraft. Flow data from the AIMMS shall be used to validate the model around the pylons. Normally, the AIMMS data is calibrated for a particular position on the aircraft by performing a series of prescribed manoeuvres that are designed to account for the position of the probe relative to the centre of the aircraft, for computing the attitude solution, and for any flow perturbations due to the aircraft. However, for this study, the AIMMS wind data was processed without the second set of calibration coefficients applied to obtain the raw air flow vector. The AIMMS data thus provides actual angle of attack (AOA) and sideslip (AOSS) as measured at the location of the probe.

## **CFD METHODOLOGY**

A full-scale solid model of the aircraft was produced from a point cloud obtained from a Leica ScanStation P20. Multiple scans of the aircraft were performed from different angles,

104 above and below the fuselage, while the aircraft was positioned in the hanger, yielding a complete  
105 and comprehensive point cloud. The expected accuracy of the scan was  $\pm 3\text{mm}$  as specified in  
106 the manufacturer data sheet. Following the scan, the data was transferred to Leica Geosystems  
107 Cyclone software which, with a 2mm constraint, allowed registration and unification of the multiple  
108 point clouds into a single dataset. The file was finally output as an STL file for inputting into the  
109 Computer Aided Design (CAD) package CATIA.

110 CATIA was used to produce a series of surfaces defined through curves generated from the  
111 point cloud. Where possible, multiple surfaces were concatenated to minimise the total number of  
112 surfaces used to describe the aircraft. Finally, the CATIA solid model was outputted as an IGES  
113 file for importing into the meshing software ANSYS ICEM CFD. Table 1 summarises the key  
114 dimensions of the aircraft.

115 ANSYS ICEM CFD was used to generate an unstructured mesh via the octree method, consisting  
116 of tri surface elements and tetra volume cells. Smoothing was subsequently applied to increase  
117 the overall mesh quality. Several mesh densities were produced in order to refine the model, the  
118 coarsest of which had 6 million cells and the finest 15 million. The cylindrical domain was specified  
119 with 10 times the characteristic length of the aircraft downstream, 5 times the characteristic length  
120 upstream, and 5 times the characteristic length for the radius. A mesh refinement study Delise  
121 (2017) revealed that a mesh with fine detail on and around the pylons and canisters, but relatively  
122 low density elsewhere (12.5 million cells in total) provided adequate accuracy in terms of lift and  
123 drag coefficients, as well as flow angles and velocities upstream of the canisters, compared to finer  
124 density meshes. The model was created without probes installed in the canisters. The ends of the  
125 canisters have been blanked with hemispherical domes and these are included in the model.

126 As is conventional for high speed compressible flows MacCormack (1981), solutions were  
127 sought via an implicit, steady state, density based solver in ANSYS Fluent v16 for all cases.  
128 Simulation parameters were specified to represent cruise conditions for which reliable flight-test  
129 data had previously been acquired, see Table 2.

130 Adequate convergence of the solutions was considered when RMS perturbations of the lift and

drag coefficients were less than  $1 \times 10^{-4}$ , Roache (1998). This was achieved by initially specifying a first order solution, and then gradually blending in the second order terms until a full second order solution had converged, and was typically achieved in approximately 35,000 iterations.

Prior to conducting the full matrix of CFD simulations using the developed model, two test cases were analysed to understand if the model could be simplified while still maintaining representative flow angles in the vicinity of the probe measurement location. A plot line is defined, see Fig. 2, to analyse the air flow upstream of the AIMMS. The line is coaxial with the boom on which the probe is installed, but extends further into the upstream airflow approximately 12m. The flow angle analysis followed the same methodology as in a previous publication regarding the response of angle of attack and sideslip angle vanes fitted to the nose of a Jetstream 31 Bennett et al. (2017a,b). The following two subsections discuss the effect on the air flow angles when the engine is in operation, and also the use of viscous/inviscid solvers.

### **Engine Operative and Inoperative Comparison**

Analysis was undertaken to quantify the effect of the turbofan engines on the flow characteristics in the vicinity of the AIMMS probe. The CFD model incorporates two disks at the inlet and outlet of the engines. Isentropic flow theory Massey and Ward-Shith (1998) was used to estimate the pressure jump through the nozzle, assuming that in cruise conditions ( $M \approx 0.5$ ) the engine inlet is at 95% atmospheric pressure with inlet velocity of  $M \approx 0.2$ , and at the outlet the flow is accelerated to  $M \approx 0.9$  to give a pressure recovery of 96% of the atmospheric value. Based on typical combustion temperatures and pressures for the Lycoming ALF-507-1H turbofan engine used on this aircraft, and the physical dimensions obtained from scale drawings, the pressure at the outlet was calculated to be approximately 60,000Pa and the temperature 345K. The inlet and outlet conditions were defined as pressure inlet and outlet boundary conditions in the Fluent case files.

Fig. 3 shows a comparison of the air flow angles, along the plot line shown in Fig. 2, for the engine in operation and inoperative at  $5^\circ$  AOA and  $0^\circ$  AOSS; note that compared to typical airliner operation, this is a relatively high AOA because the FAAM aircraft typically operates close to best endurance speed (termed ‘Science Speed’) rather than slightly above best range speed. It is seen that

at  $x = 0$  the air flow approaches the free stream conditions (AOA (x-z plane) =  $5^\circ$ , AOSS (x-y plane) =  $0^\circ$ ). As  $x$  increases, the upwash associated with the wing's leading edge gradually intensifies (positive flow in the x-z plane) with an associated outboard flow (negative flow in the x-y plane) due to the swept and tapered nature of the wing. From  $x \approx 0.7$ , the flow angle changes radically as other parts of the aircraft exert an influence on the airflow. There is a turning point at  $x \approx 0.73$  due to the geometry of the engine cowl/casing which causes the upwards and outboard flows to weaken in magnitude. The vertical and horizontal flow angles then further increase dramatically at  $x \approx 0.95$  and  $x \approx 0.85$  respectively to the stagnation point at the canister dome. It is seen that at the AIMMS measurement location, for this particular case, the vertical flow angle has been reduced and the horizontal flow forced outboard compared to the free stream condition.

Comparing the solid and dotted lines in Fig. 3, it is seen that the engine's operation has minimal effect on the flow angle in the x-z (vertical) plane, but causes a reduction in flow angle in the x-y (transverse) plane in the vicinity of the AIMMS probe pressure ports of approximately  $1.5^\circ$ . Hence, it was concluded that the engine's operation should be included in the full matrix of CFD simulations going forwards.

### Viscous and Inviscid Solver Comparison

For the flight envelope considered in this paper, as seen in Table 2, the Reynolds numbers are of magnitude  $10^7$ . At high Reynolds number conditions such as these, the turbulent boundary layer on the probe is calculated to grow up to approximately 8mm (using  $\delta \approx 0.37x/\text{Re}_x^{1/5}$  where  $x = 0.425\text{m}$  is the length of the probe,  $\text{Re}$  is calculated based on the conditions given in Table 2, and a zero pressure gradient is assumed due to the constant diameter of the probe boom) and hence would not affect the airflow at the other three instrument positions as there is a minimum horizontal/vertical separation of 0.56m. Furthermore, due to the length of the probe boom, the measurement location is well upstream of any congestion effects caused by the stagnation point on the canister dome, as discussed by Korolev in Korolev et al. (2012).

Fig. 4 shows a comparison of the flow angles, along the plot line in Fig. 2, for inviscid and viscous solutions at  $5^\circ$  AOA and  $0^\circ$  AOSS. The plots, in general, exhibit the same characteristics

as in Fig. 3. Comparing the solid and dashed lines, it is seen that the results are well matched, differing by a maximum of  $0.1^\circ$  across the observed range. Therefore, it is concluded that the use of an unstructured mesh with inviscid solver provides sufficiently accurate and representative results compared to a fully structured mesh with prism layers treated with the Spalart-Allmaras turbulence model. This allowed significant computational expense can be spared by reducing the size of the mesh due to the omission of the prism layers, and using an inviscid solver in Fluent.

### **Anti-Icing Vents**

It is worth noting that the aircraft has anti-icing vents on the underside of the wings. This is essentially a bleed air system which routes hot air from the engines to outlets on the lower surface of the wings. Although the air is exhausted upstream of the probe location at approximately  $200^\circ\text{C}$ , it is assumed that the flow rate is not high enough to affect the airflow onto the probe, which is positioned approximately 1m below the wing.

### **Final Model and Identification of Comparable Flight Test data**

In the subsections above, justification for inclusion of the engine effects, but using an unstructured mesh with inviscid solver, is confirmed. It was assumed, therefore, that the main factors affecting the airflow direction and velocity at the AIMMS probe measuring location are the engine effects, redirection/deflection of airflow around the airframe, and the pressure field generated by the wing.

To investigate fully, a matrix of CFD simulations were specified with appropriate conditions to collate the final set of results with which to compare to flight test data. AIMMS data from flight B875 was used for the validation of the final CFD model. This flight took place on 28 November 2014 off the north west coast of Scotland. Three suitable straight and level runs were identified with average altitudes of 88m ( $\sim 300\text{ft}$ ), 7,610m ( $\sim 25,000\text{ft}$ ), and 10,271m ( $\sim 33,700\text{ft}$ ) with the CFD model validation work been done using static conditions for 7,610m ( $\sim 25,000\text{ft}$ ). At this altitude, 4 hrs and 10 mins into the flight, and with these flight conditions the relationship between AOA as measured by the radome 5-port turbulence probe and TAS was found and shown in Table 2.



The x-axis reference for the CFD model is parallel to the aircraft seat rail datum, this reference is also used by the on-board GPS-aided Inertial Navigation system which records aircraft pitch during flight. Comparisons of the model and AIMMS data is presented in terms of AOA and to ensure that the aircraft AOA was the same as the model AOA, the pitch was plotted against AOA as measured with the nose-mounted turbulence probe (assumed to be free of flow distortions). The slope of the fit was found to be 1.02 with an  $r^2$  value of 0.93 for the 7,610m (~ 25,000ft) flight leg. Therefore, the modelled AOA at the AIMMS location and the AOA measured by the AIMMS probe, are comparable.

## RESULTS

The CFD results are compared to the in-flight AIMMS data for comparable conditions in Fig. 5. The x-axis displays the ‘true’ AOA, and the y-axis displays the ‘measured’ AOA at the AIMMS probe, for each set of data. For the case of the CFD data, the ‘true’ AOA is given by the simulation set-up flow angle. For the case of the flight test data, the ‘true’ AOA is provided by the 5-hole probe located in the radome. It is also worth stating that the flight test data has been shifted by  $3.1^\circ$  to match the fuselage reference line used in the CFD simulations since the AIMMS canister has been mounted on the aircraft  $3.1^\circ$  nose-down relative to the aircraft datum. Furthermore, the flight test data has been filtered to contain only data points with  $\pm 0.2^\circ$  AOSS. The linear fit of the flight data has a slope of 1.32 compared to 1.56 for the model, with  $r^2=0.95$ . Also, 95% confidence intervals have been added to each set of data. The confidence interval for the CFD results also includes a potential error due to the  $\pm 3$ mm accuracy of the laser scan used to generate the aircraft model.

Both sets of data show that the air flow angle in the vicinity of the AIMMS probe is decreased as compared to the freestream value. As discussed above, this effect is understood to be due to the engines, redirection/deflection of the airflow around the aircraft, and the pressure field generated below the wing with associated upwash. Fig. 6 shows two different cut plane pressure contours (x-z upper and x-y lower) to illustrate this. The measurement location of the AIMMS probe clearly lies within a region of high pressure caused by a combination of effects: the port outer engine’s operation, the wing generating lift, the redirection/deflection of air flow around the engine casing.

It is seen from Fig. 5 that the CFD results provide good consistency, with confidence intervals of approximately  $\pm 0.1^\circ$ . The filtered flight test data also exhibits minimal scatter, giving confidence intervals of approximately  $\pm 0.2^\circ$ . This was the primary reason for selecting the data set at 7,610m (~25,000ft); The data was evidently much less susceptible to scatter due to turbulence, for example. The uncertainty of individual AOA measurements of the AIMMS has not been included in the calculation of the confidence intervals.

The CFD model performs well despite, in general, over predicting the AIMMS probe flow angle within the flight test range up to a maximum of  $0.28^\circ$ . The CFD prediction is most accurate at the lower end of the flight test range, around  $4.6^\circ$  angle of attack, where the two lines of best fit intersect. However, since the CFD and flight test data trend lines have a gradients of 1.56 and 1.32 respectively, the prediction diverges at the higher angle of attack range. Despite this, for a typical flight condition, for example 7,610m (~25,000ft),  $5^\circ$  AOA, and  $0^\circ$  AOSS, the CFD model over predicts the flow angle at the AIMMS probe by just  $0.09^\circ$ . The discrepancy in the results may in part be due to inaccuracy of the 5-hole probe in the radome, which is assumed here to provide a 'true' AOA for the flight test data. Without the benefit of a boom style AOA sensor, or specific data regarding the accuracy of the 5-hole probe, the results must rely on this assumption.

The flow velocity perturbations for all four of the canister positions were found using the CFD model for a range of AOA at 7,610m (~25,000ft). Fig. 7(a) plots the longitudinal velocity scaling relative to TAS and shows a slowing of the free-stream velocity for all positions, the magnitude of which increases with AOA. The canisters experience a decrease of 3-12% in longitudinal flow velocity across the operating conditions. The transverse velocity perturbations have opposite signs for canisters on either side of the pylon. Inboard canisters experience a flow towards the fuselage, positive values in Fig. 7(b), due to the influence of the engine cowling, while there is a flow towards the wing tip at the outboard canisters. The free-stream horizontal component is zero (AOSS= 0) while the perturbed flows vary by approximately 12% of TAS, that is  $\pm 6\text{m/s}$  transverse flows for a TAS of  $100\text{m/s}$ , or  $\pm 19\text{m/s}$  at  $150\text{m/s}$ . The vertical flow perturbation (not shown) is always negative, due to the influence of the wing, with the upper canister positions experiencing perturbations of

9-10% of TAS compared to 5-7% for the lower positions. The cowling and nacelle also exert an influence in the x-z plane, vertical flows at the inner canister positions having approximately 1% less downward perturbation than at the outer positions. It should be noted that the flow disturbances here are due only to the influence of the aircraft, the effect of the probes themselves is not included. The design of the probes has been shown to have a significant compressive effect on the flow through the sample volume but this depends on the design of the individual probes Weigel et al. (2016). Inclusion of this effect is beyond the scope of the presented work however the perturbations due to the probe itself may be comparable to those caused by the airframe for several common probe types, that is approximately 5% Korolev et al. (2012). Weigel et al. Weigel et al. (2016) present measured perturbations of greater than 20% which include the effect of both the aircraft, in their case a Gulfstream G-550, and the probes. The canister position relative to the wing and engine cowling means that probes in different positions will experience different flows. Particles of different sizes shall be affected by the different flow vectors and the implementation of particle flow into the CFD model is a subject of ongoing work.

## **IMPACT OF AIR FLOW ON OPTICAL ARRAY PROBES**

Optical array probes were developed Knollenberg (1970) to determine the particle size distribution and shape of cloud and precipitation particles. Particles pass through an expanded laser beam and the shadow cast is measured on a one dimensional array. The array is read on a nanosecond time scale with the detector clock frequency and the particle/air speed through the laser beam determining the longitudinal resolution of the probe. The transverse resolution is determined by the pixel size and magnification of the imaging optics and may range from  $10\mu\text{m}$  to  $150\mu\text{m}$  depending on the probe.

A simple model has been made that digitises an arbitrarily-shaped particle with a 64 pixel linear array, the array size used in the Droplet Measurement Technologies Cloud Imaging Probe (CIP) as flown on the aircraft. The model particle can be stretched and skewed to simulate a particle carried through the probe sample volume with a perturbed airspeed and direction. Fig. 8 shows a spherical water droplet and the image produced by a  $15\mu\text{m}$  resolution CIP for both the unperturbed

293 airflow case and the case when there is a -20% change in the longitudinal and a 10% change in  
294 the transverse airflows. The degree of perturbation may be larger than realistic but has been used  
295 for visual clarity in both Figs. 8 and 9. The circle is both stretched, due to the particle passing  
296 through the sample volume more slowly, and skewed, due to the particle passing through the sample  
297 volume at an angle. The standard operating orientation of the CIPs on the aircraft is with the arms  
298 vertical. The transverse flow perturbations of interest in this case are thus horizontal. With the  
299 arms horizontal, the vertical airflow perturbations would be relevant.

300 The two dimensional image measured by the CIP is used to classify the three dimensional  
301 size and shape of the particle and there are a number of common methods for allocating a size  
302 to a particle of arbitrary shape Korolev and Isaac (2003); Wu and McFarquhar (2016). Fig. 9  
303 shows a synthetic hexagonal plate undergoing the same flow perturbations and sampling as for  
304 Fig. 8 and superimposed on the image are some common particle size definitions. The maximum  
305 transverse length, which is the maximum length in the plane of the photodiode array and shown  
306 as  $D_P$ , maximum longitudinal length, or length in the time dimension and shown as  $D_T$ , the  
307 hypotenuse of these two lengths,  $D_H$ , maximum length in any orientation,  $D_{\max}$ , and the length  
308 in the direction orthogonal to  $D_{\max}$ ,  $D_w$ , are common linear measurements. The diameter of the  
309 minimum enclosing circle,  $D_S$ , and the diameter of the area-equivalent circle,  $D_A$ , are also common  
310 and all are used to determine cloud and precipitation particle size distributions. The form of the  
311 reported size distribution shall be dependent on the definition used but importantly, may also be  
312 shifted due to any aforementioned image stretch and/or skew that has not been accounted for in the  
313 post-processing.

314 In order to illustrate the effect of stretch and skew, Fig. 10 shows the size scaling factor; that is  
315 the ratio of reported size for a perturbed particle image to that of the unperturbed particle image,  
316 of a spherical droplet as a function of longitudinal stretch and transverse skew. The scaling factor  
317 was found by performing a Monte-Carlo simulation with randomized size scaling and rotation  
318 of the same synthetic particle image. The results shown are for a droplet as this is the simplest  
319 case, however the same process was applied to a square, hexagonal plate (Fig. 9), a six-sided star

(approximating a dendrite), a rectangle (with aspect ratio 15:1 to approximate an ice needle), and an ice aggregate based on a real particle image presented in Wu and McFarquhar (2016). For the longitudinal perturbation shown in Fig. 10(a), the transverse size,  $D_P$ , is unchanged however the longitudinal dimension,  $D_T$ , and the area equivalent diameter are. A similar, approximately 1:1 linear trend is seen when changing the clock frequency of a CIP in the laboratory as metallic circular dots are passed through the sample volume at constant speed. This is presented in terms of aspect ratio,  $D_T/D_P$ , by Weigel et al. (2016) and is the inverse of a constant clock frequency while the air/particle speed through the instrument changes. Fig. 10(b) shows the impact of a transverse perturbation on the same size parameters. Here, the fractional change in size is significantly smaller and so the effect of digitization makes the data noisy. This is fortunate as this perturbation is significantly more difficult to account for. Some instruments include a pitot tube for local measurement of the PAS, this however does not measure transverse flow components. With randomized orientation, the average behaviour of shapes with an aspect ratio close to unity approaches that of a circle as the number of samples in the Monte-Carlo simulation increases. For the needle and aggregate however, a transverse perturbation results in a reduction in the apparent size of the particles of up to 2% for a 10% transverse velocity change. Thus the shape of the particle being measured by the probe shall effect the magnitude of any mis-sizing depending on the sizing metric being used.

## CONCLUSIONS

CFD techniques have been used to predict the air flow characteristics in the vicinity of instruments fitted to underwing pylons on the FAAM BAe-146 atmospheric research aircraft (ARA). Data from the AIMMS at 7,610m (~25,000ft) during flight B875 was used to validate the model for a range of air speeds and AOA and show good agreement to within  $0.25^\circ$  on average and a gradient difference within 15%. Having validated the CFD model, the results were used to determine the flow perturbations due to the aircraft at all of the pylon instrument positions. Each of the positions experience different perturbations which also vary with aircraft AOA. Longitudinal flows slowed by a maximum of 12% while a transverse flow of up to  $\pm 6\%$  of TAS was introduced, with the sign

switching between inboard and outboard positions.

Influence of perturbation of the flows on cloud particle measurements was examined with a simple imaging probe simulation. Uncorrected changes in the longitudinal flow velocity can introduce particle size scaling, in the worst case relative changes in measured size may be as large as the relative change in velocity depending on the sizing metric used. The influence of the transverse perturbation is significantly less with size scaling of only up to 0.5% for realistic flight conditions. This is significantly less than other measurement uncertainties of the technique. Obtaining the flow perturbations from a CFD model at the measurement locations will improve accuracy of particle size measurements or at least improve understanding of sizing uncertainties.

Future enhancements to the study shall introduce particles into the flow model with the inclusion of accurate probe geometries (rather than modelling the canisters with a domed blank), and utilise a viscous model. To enable the analysis of the near-field effects in more detail. Additionally, a sensitivity study of the model is recommended to analyse the effect of altitude, airspeed, AOA, and AOSS on the flow perturbations introduced, so that the flows, and their effect on under-wing particle measurements, can be calculated for a broad range of applicable flight conditions.

## REFERENCES

- Bennett, C. J., Lawson, N. J., Gautrey, J., and Cooke, A. (2017a). “CFD simulation of flow around angle of attack and sideslip angle vanes on a BAe Jetstream 3102 - part 1.” *Aerospace Science and Technology*, 68, 561–576.
- Bennett, C. J., Lawson, N. J., Gautrey, J., and Cooke, A. (2017b). “CFD simulation of flow around angle of attack and sideslip angle vanes on a BAe Jetstream 3102 - part 2.” *Aerospace Science and Technology*, 68, 577–587.
- Delise, M. (2017). “Investigation of the turbofan jet effect upon the measurement canisters of the FAAM BAe 146-301.” M.S. thesis, Cranfield University, UK.
- Knollenberg, R. G. (1970). “The optical array: An alternative to scattering or extinction for airborne particle size determination.” *Journal of Applied Meteorology*, 9, 86–103.
- Korolev, A., Emery, E., and Creelman, K. (2012). “Modification and tests of particle probe tips to mitigate effects of ice shattering.” *Journal of Atmospheric and Oceanic Technology*, 30(4), 690–708.
- Korolev, A. and Isaac, G. (2003). “Roundness and aspect ratio of particles in ice clouds.” *Journal of Atmospheric Sciences*, 60(15), 1795–1808.
- MacCormack, R. W. (1981). “A numerical method for solving the equations of compressible viscous flows.” *AIAA*, 20(9), 1275–1281.
- MacPherson, J. and Baumgardner, D. (1988). “Airflow about King Air wingtip-mounted cloud particle measurement probes.” *Journal of Atmospheric and Oceanic Technology*, 5, 259–273.
- Massey, B. and Ward-Shith, J. (1998). *Mechanics of Fluids - Seventh Ed.* Nelson Thornes Ltd., UK.
- Roache, P. J. (1998). *Verification and Validation in Computational Science and Engineering.* Hermosa, New Mexico, USA.

- Twohy, C. and Rogers, D. (1993). “Airflow and water-drop trajectories at instrument sampling points around the Beechcraft King Air and Lockheed Electra.” *Journal of Atmospheric and Oceanic Technology*, 10, 566–578.
- Weigel, R., Spichtinger, P., Mahnke, C., Klingebiel, M., Afchine, A., Petzold, A., Kramer, M., Costa, A., Molleker, S., Reutter, P., Szakall, M., Port, M., Grulich, L., Jurkat, T., Minikin, A., and Borrmann, S. (2016). “Thermodynamic correction of particle concentrations measured by underwing probes on fast-flying aircraft.” *Atmospheric Measurement Technology*, 9, 5135–5162.
- Wilson, J. C. and Jonsson, H. (2011). “Measurement of cloud and aerosol particles from aircraft.” *Aerosol Measurement: Principles, Techniques, and Applications*, P. Kulkarni, P. A. Baron, and K. Willeke, eds., John Wiley & Sons, 3rd edition, 655–665.
- Wu, W. and McFarquhar, G. (2016). “On the impacts of different definitions of maximum dimension for nonspherical particles recorded by 2D imaging probes.” *Journal of Atmospheric and Oceanic Technology*, 33, 1057–1072.



399

## List of Tables

400

1 Key dimensions of the aircraft. . . . . 18

401

2 CFD model test conditions based on typical scientific flight conditions. . . . . 19

Aircraft Section	Size
Total Aircraft Length (m)	14.31
Wing Span (m)	15.83
Wing Tip Chord (m)	0.83
Tail Span (m)	6.61
Tail Tip Chord (m)	0.65
Fin Tip Chord (m)	0.84
Wing Gross Area (m <sup>2</sup> )	25.60
Aspect Ratio	9.79

**TABLE 1.** Key dimensions of the aircraft.

Parameter	Value
Angle of Attack*, $\alpha$ (°)	3.5 - 6
Slideslip Angle, $\beta$ (°)	-5 - 5
True Airspeed, TAS (m/s)	142.17 - 171.92
Mach Number, M	0.46 - 0.56
Reynolds Number, Re	$1.51 \times 10^7$ - $1.82 \times 10^7$
Altitude (ft)	25,000
Air Density (kg/m <sup>3</sup> )	0.55
Temperature (°C)	239
Pressure (Pa)	37600
*AOA=17.3-0.08(TAS)	over 3.5-5.5° range

**TABLE 2.** CFD model test conditions based on typical scientific flight conditions.

## List of Figures

- 1 Port side underwing instrument canisters on the aircraft. . . . . 22
- 2 Plot line for the flow angle and velocity magnitude comparisons for viscous/inviscid analysis in Fig. 4, and the engine operative/inoperative analysis in Fig. 3 . . . . . 23
- 3 Comparison of flow angles upstream of the canister dome for engine operative and inoperative cases ( $AOA=5^\circ$ ,  $AOSS=0^\circ$ ). The x-axis is normalised with respect to the length of the plot line, Fig. 2. . . . . 24
- 4 Comparison of the flow angles upstream of the canister dome for inviscid and viscous solutions ( $AOA=5^\circ$ ,  $AOSS=0^\circ$ ). The x-axis is normalised with respect to the length of the plot line, Fig. 2. . . . . 25
- 5 Comparison of flight test and CFD (at comparable flight conditions) predicted AOA (x-z plane) flow angles with reference line correction (Flight test data filtered to include only points with  $\pm 0.2^\circ$  AOSS) and 95% confidence intervals applied. . . . 26
- 6 Pressure contours (x-y plane upper, x-z plane lower) showing areas of high pressure below the wing, behind the engine casing, and on the canister domes, in relation to the AIMMS Probe measurement location. . . . . 27
- 7 Flow perturbation as a function of TAS in the (a) longitudinal and (b) horizontal from the free-stream conditions as a function of aircraft AOA. Results are shown for each of the four canister positions on each under-wing pylon but do not include the effect of the canisters themselves. . . . . 28
- 8 The source simulated spherical droplet with digitized CIP images for both the unperturbed airflow case and the case when there is a -20% change in the longitudinal and a 10% change in the transverse airflows. These changes are large but used so that the effect on the particle image is more obvious. . . . . 29
- 9 Simulated hexagonal plate and associated CIP images. Marked are common measures of particle size, see the text for details. . . . . 30

428	10	Effect on the reported size of a spherical droplet for (a) longitudinal flow velocity	
429		perturbations and (b) transverse flow velocity perturbations from the free-stream	
430		conditions. The sizing definitions are described in the text. The effect of the	
431		transverse velocity, presented as a fraction of the TAS, is small so that there is	
432		significant noise associated with digitization. . . . .	31

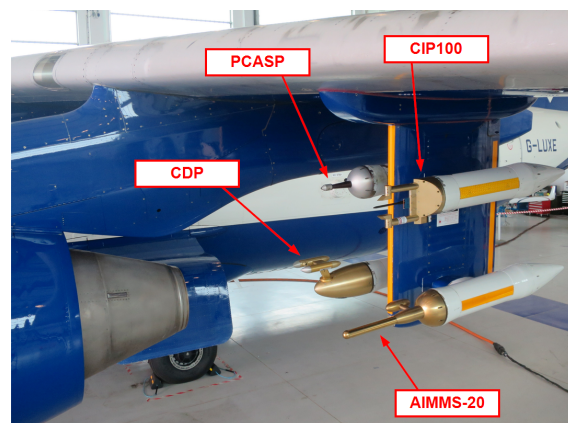
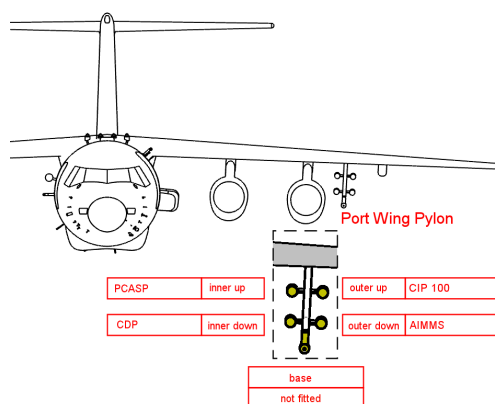


**Fig. 1.** Port side underwing instrument canisters on the aircraft.

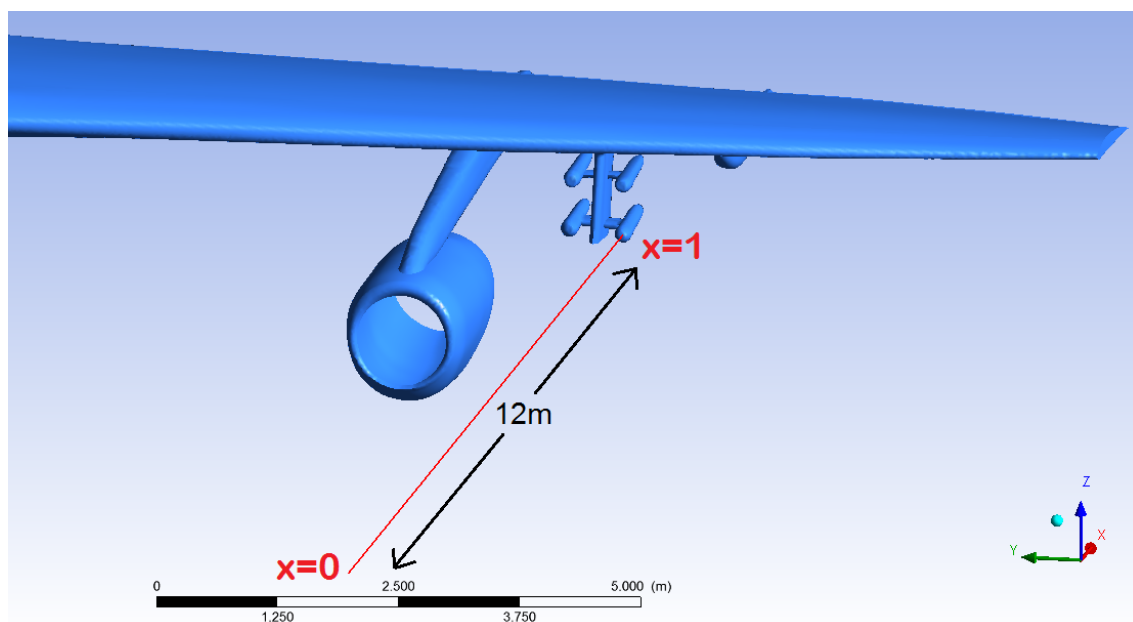


**Fig. 2.** Plot line for the flow angle and velocity magnitude comparisons for viscous/inviscid analysis in Fig. 4, and the engine operative/inoperative analysis in Fig. 3

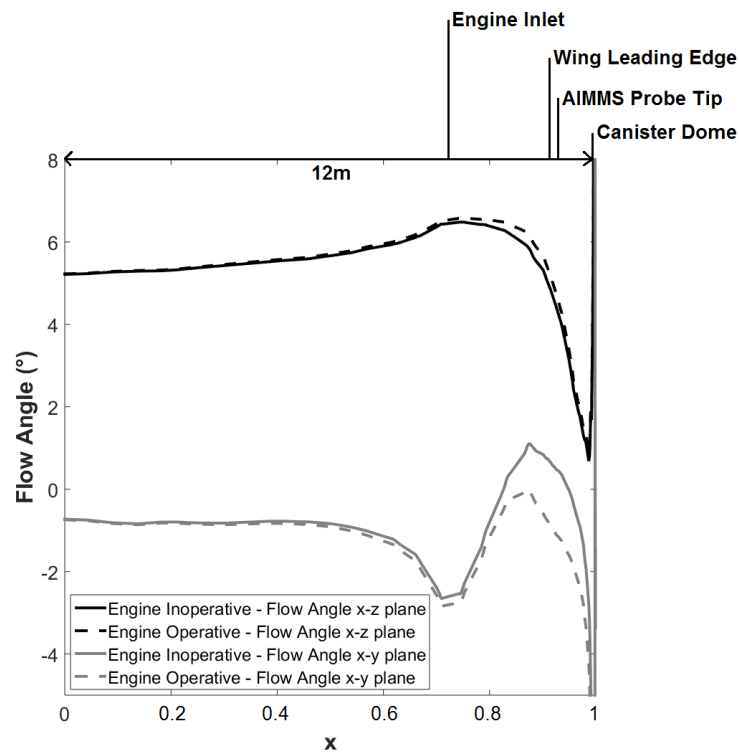


**Fig. 3.** Comparison of flow angles upstream of the canister dome for engine operative and inoperative cases ( $AOA=5^\circ$ ,  $AOSS=0^\circ$ ). The x-axis is normalised with respect to the length of the plot line, Fig. 2.



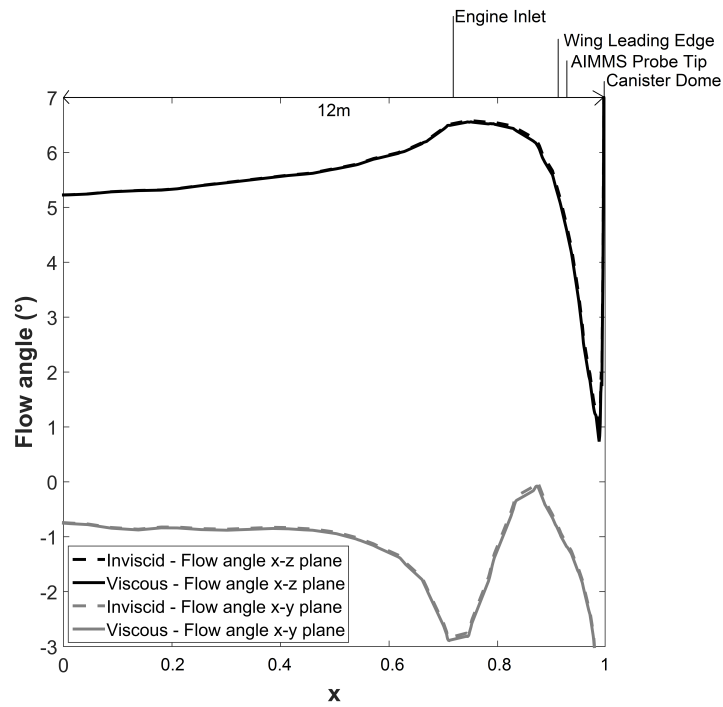


**Fig. 4.** Comparison of the flow angles upstream of the canister dome for inviscid and viscous solutions ( $AOA=5^\circ$ ,  $AOSS=0^\circ$ ). The x-axis is normalised with respect to the length of the plot line, Fig. 2.

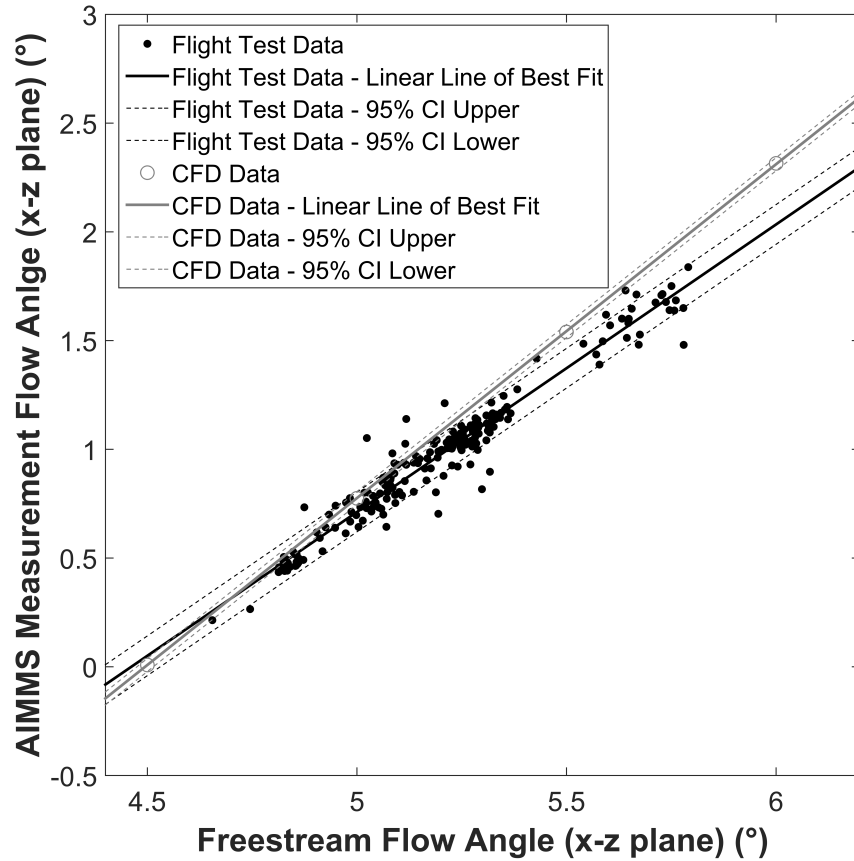


**Fig. 5.** Comparison of flight test and CFD (at comparable flight conditions) predicted AOA (x-z plane) flow angles with reference line correction (Flight test data filtered to include only points with  $\pm 0.2^\circ$  AOSS) and 95% confidence intervals applied.

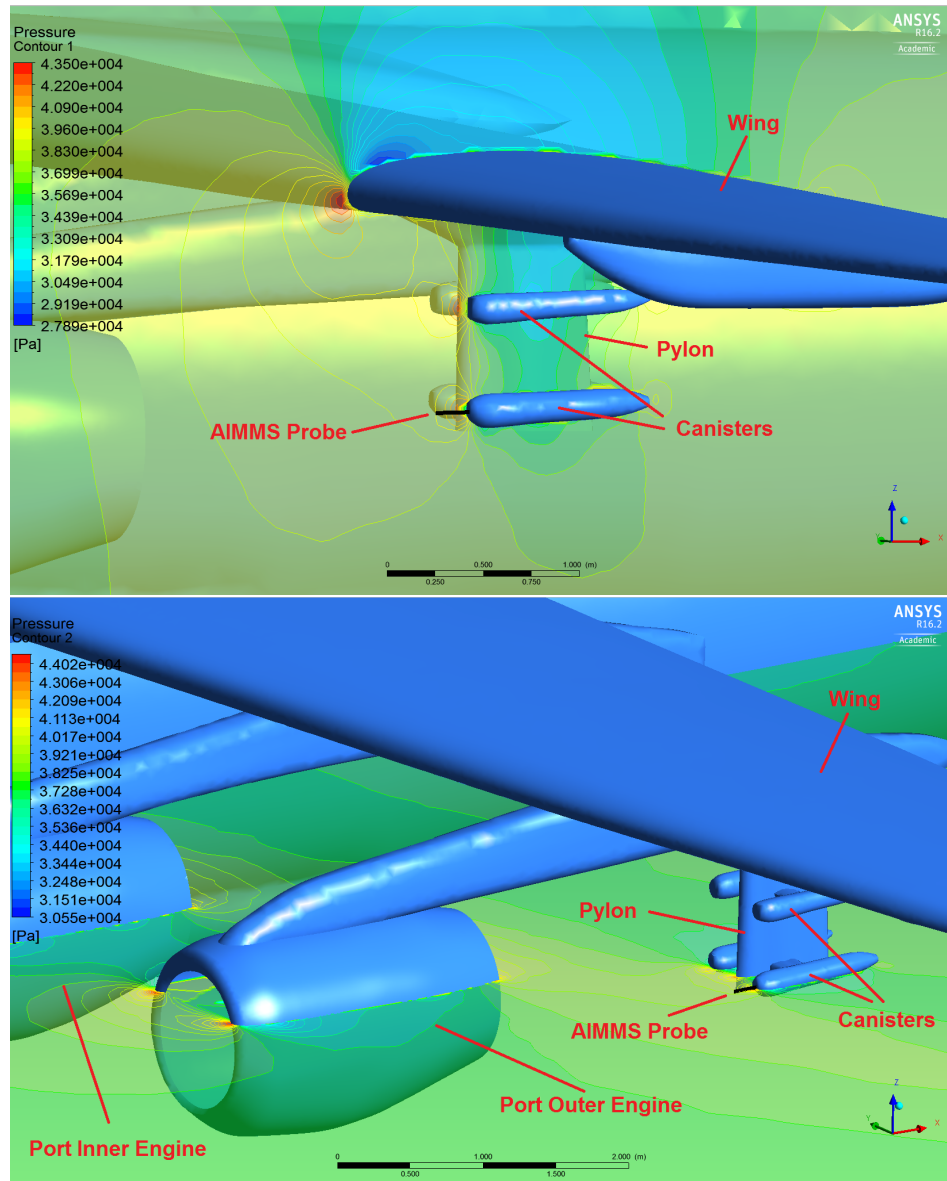


**Fig. 6.** Pressure contours (x-y plane upper, x-z plane lower) showing areas of high pressure below the wing, behind the engine casing, and on the canister domes, in relation to the AIMMS Probe measurement location.

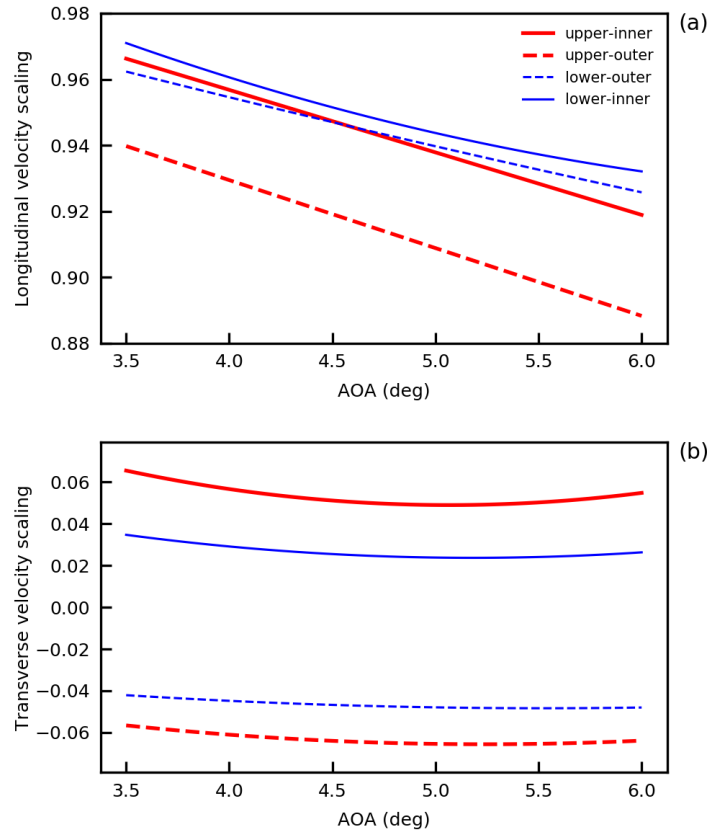


**Fig. 7.** Flow perturbation as a function of TAS in the (a) longitudinal and (b) horizontal from the free-stream conditions as a function of aircraft AOA. Results are shown for each of the four canister positions on each under-wing pylon but do not include the effect of the canisters themselves.

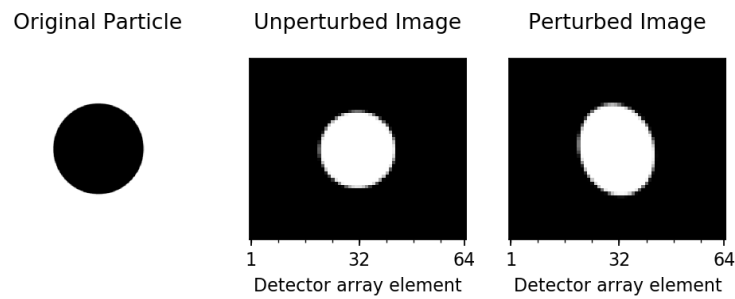


**Fig. 8.** The source simulated spherical droplet with digitized CIP images for both the unperturbed airflow case and the case when there is a -20% change in the longitudinal and a 10% change in the transverse airflows. These changes are large but used so that the effect on the particle image is more obvious.

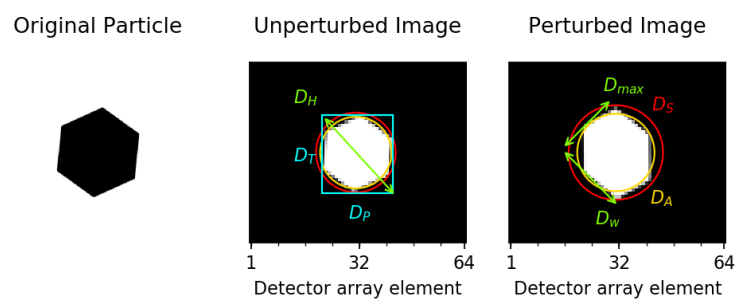


**Fig. 9.** Simulated hexagonal plate and associated CIP images. Marked are common measures of particle size, see the text for details.

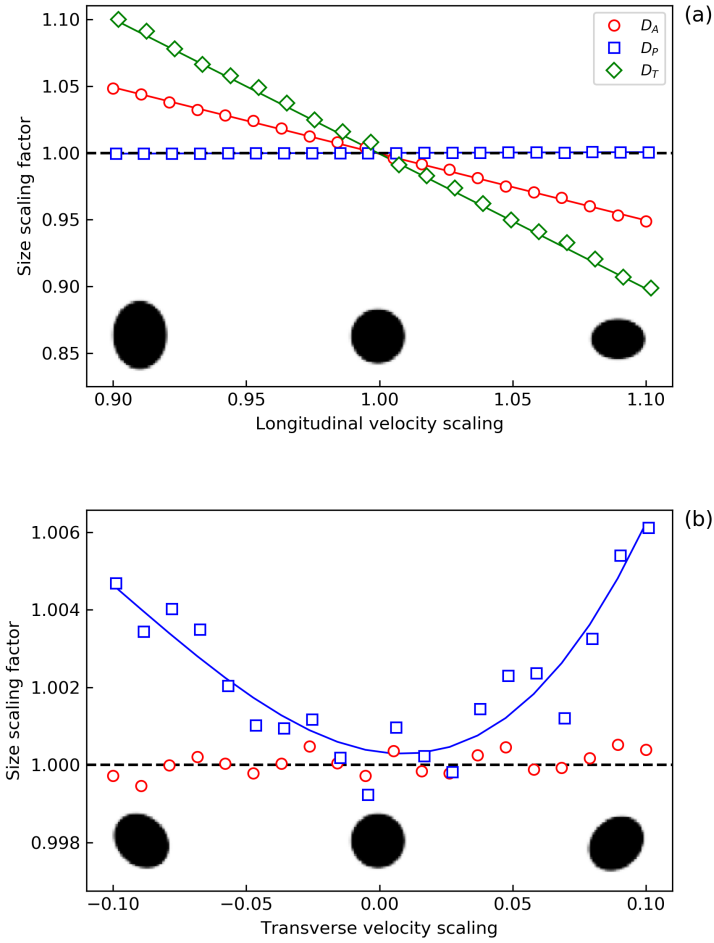


**Fig. 10.** Effect on the reported size of a spherical droplet for (a) longitudinal flow velocity perturbations and (b) transverse flow velocity perturbations from the free-stream conditions. The sizing definitions are described in the text. The effect of the transverse velocity, presented as a fraction of the TAS, is small so that there is significant noise associated with digitization.

2019-04-30

# Characterizing instrumentation canister aerodynamics on the FAAM BAe-146-301 atmospheric research aircraft

Bennett, Christopher J.

ASCE

---

Bennett CJ, Nott GJ, Wellpott A, Lawson N, Delise M, Woodcock B and Gratton GB.

Characterising instrumentation canister aerodynamics on the FAAM BAe-146-301 atmospheric research aircraft. Journal of Aerospace Engineering, Volume 32, Issue 4, 2019

[https://doi.org/10.1061/\(ASCE\)AS.1943-5525.0001044](https://doi.org/10.1061/(ASCE)AS.1943-5525.0001044)

*Downloaded from Cranfield Library Services E-Repository*